remote sensing

MDPI

Article

A Combination of Classification Robust Adaptive Kalman Filter with PPP-RTK to Improve Fault Detection for Integrity Monitoring of Autonomous Vehicles

Hassan Elsayed [1,2], Ahmed El-Mowafy [1,*], Amir Allahvirdi-Zadeh [1], Kan Wang [3,4,5] and Xiaolong Mi [6]

1 School of Earth and Planetary Sciences, Curtin University, Perth 6102, Australia; hassan.elsayed@curtin.edu.au (H.E.); amir.allahvirdizadeh@curtin.edu.au (A.A.-Z.)
2 Faculty of Engineering, Suez Canal University, Ismailia 41522, Egypt
3 National Time Service Center, Chinese Academy of Sciences, Xi'an 710600, China; wangkan@ntsc.ac.cn
4 University of Chinese Academy of Sciences, Beijing 100049, China
5 Key Laboratory of Time Reference and Applications, Chinese Academy of Sciences, Xi'an 710600, China
6 Department of Land Surveying and Geo-Informatics, The Hong Kong Polytechnic University, Hong Kong; xiaolong.mi@polyu.edu.hk
* Correspondence: a.el-mowafy@curtin.edu.au

Abstract: Real-time integrity monitoring (IM) is essential for autonomous vehicle positioning, requiring high availability and manageable computational load. This research proposes using precise point positioning real-time kinematic (PPP-RTK) as the positioning method, combined with an improved classification adaptive Kalman filter (CAKF) for processing. PPP-RTK enhances IM availability by allowing undifferenced and uncombined observations, enabling individual observation exclusion during fault detection and exclusion (FDE). The CAKF reduces FDE computational load by using a robustness test instead of traditional FDE methods, improving precision and availability in protection level estimation. Epoch-wise weighting adjustments in the robustness test create a more accurate stochastic model, aided by an adaptive unit weight variance (UWV) calculated with a sliding window, achieving a 7–28% UWV reduction. Three test scenarios with up to four simultaneous faults in code and phase observations, ranging from 1 to 200 m and 0.4 to 20 m, respectively, demonstrated successful identification and de-weighting of faults, resulting in maximum positioning errors of 6 mm (horizontal) and 11 mm (vertical). The method reduced FDE computational load by 50–99.999% compared to other approaches.

Keywords: integrity monitoring; fault detection and identification; autonomous vehicles; PPP-RTK; robust estimation; adaptive Kalman filter

Academic Editor: Gino Dardanelli

Received: 24 November 2024
Revised: 3 January 2025
Accepted: 9 January 2025
Published: 15 January 2025

Citation: Elsayed, H.; El-Mowafy, A.; Allahvirdi-Zadeh, A.; Wang, K.; Mi, X. A Combination of Classification Robust Adaptive Kalman Filter with PPP-RTK to Improve Fault Detection for Integrity Monitoring of Autonomous Vehicles. *Remote Sens.* **2025**, *17*, 284. https://doi.org/10.3390/rs17020284

1. Introduction

Real-time precise positioning using global navigation satellite systems (GNSS) is crucial for ground applications such as autonomous vehicle (AV) operations, as it enables accurate navigation and decision making [1]. However, ensuring the integrity of the vehicle's position estimates in real time is of utmost importance to maintain safety and reliability [2,3]. Monitoring the integrity of the estimated position faces many obstacles including validation, availability and computational load [4–6]. Selecting a suitable positioning method and processing strategy can assist in overcoming some of these difficulties. For example, some applications that require real-time positioning are reliant on extended Kalman filter (EKF) for processing GNSS observations. EKF is an optimal recursive filter

that provides the minimum variance under certain conditions, which are not always met, especially in kinematic scenarios. One limitation of EKF is assuming that the system dynamic noise remains constant between epochs, potentially leading to degraded performance in changing dynamic environments [7]. AVs are an example of such kinematic scenarios, where acceleration variations and maneuvers are regularly present. This represents a challenge for EKF with a constant dynamic noise function and may cause an estimation of the state vector with low accuracy or even divergence. Due to this shortcoming, researchers have adopted an adaptive attitude for the Kalman filter in which the contribution of the time update and the measurement update will be balanced using an adaptive factor. Many methods such as adaptive estimation using multiple models, innovation adaptive estimation, and covariance scaling have been introduced to compute the adaptive factor by different means [8–12]. These methods depend on the covariance matrices of either the predicted state or the predicted residuals. All aforementioned methods provided improvements in position estimation compared to classical EKF, and some methods showed slightly better performance than the rest.

Kalman filter adaptation was examined in many studies. For example, several methods relying on Variance Component Estimation (VCE) were suggested. Although this method is shown to be effective, it is time-consuming due to the iterative process and matrix operations involved [13]. This would lead to a low performance of the application of VCE in real-time applications. Other techniques for Adaptive Kalman Filter (AKF) were through checking the quality of the observed measurements using a robustness test that adjusts the assigned variance (i.e., observation weight) for each observation. The filter in this case was named robust AKF (RKF). The test is carried out with different methods, where some are empirical and others are based on statistical testing. For instance, Yang et al. [14] suggested empirical values for the limits after which the variance of any observation will be adjusted. This approach considered all observations from different frequencies and constellations to have the same precision for the calculation of the standardized residual required for the robustness test. Zhang et al. [15] proposed a classification of the observations so that the standardized residuals can be computed separately for each observation type of different constellations, e.g., Global Positioning System (GPS) L1 code, GPS L1 phase, GPS L2 code, GPS L2 phase, etc. In addition, the robustness test was amended to rely on the *t*-test instead of empirical values based on the assumption that the standardized observation residuals and predicted residuals follow a standard normal distribution. The research of Zhang et al. [15] showed the improvement of using statistical testing instead of empirical values on the position quality using GPS and BeiDou Navigation Satellite System (BDS) measurements. The filter was named "improved classification robust adaptive Kalman filter (CAKF)". Elmezayen and El-Rabbany [16] carried out more testing scenarios based on CAKF using GPS and Galileo measurements. The study confirmed the improvements in the position quality. Lotfy et al. [17] proposed the Chi-square test as a statistical test for the robustness test. The research showed an improvement in the positioning results after using the proposed method.

Most of the previous research studies targeted the use of the precise point positioning (PPP) technique. This can be practical for some applications, but using PPP for real-time positioning of ground applications would not be an effective positioning method, as it requires a considerable convergence time to initialize or re-initialize the solution if a loss of lock takes place. This makes it a vulnerable option for applications that require instantaneous real-time positioning, especially in urban environments. Moreover, the previous studies that utilized the RKF for processing shared the same method of calculating the standardized residuals, which is a main parameter in implementing the robustness test. They used the predicted residuals, i.e., the computed residuals after the time update

step, for that purpose. Although this approach provided better results compared to EKF, the predicted residuals are still less accurate than the final residuals estimated from the best-fitting solution of the observations, i.e., after the measurement update. This can adversely affect the computed standardized residuals for each observation type. Hence, the robustness test may result in the exclusion or the de-weighting of a certain current observation unnecessarily, which may degrade positioning and IM availability. It may also lead to overlooking a necessary exclusion or de-weighting of an observation.

Due to the aforementioned shortcomings, this research suggests PPP-RTK as a positioning method, as it offers a very small convergence time compared to traditional PPP, that makes it mostly instantaneous. It also suggests processing using CAKF to enhance the IM process of real-time positioning. Using PPP-RTK as a positioning method has a significant advantage over other real-time positioning methods such as PPP, traditional RTK or Network RTK. This has been discussed broadly in Elsayed et al. [6]. In addition, PPP-RTK can enhance IM availability by exploiting the undifferenced and uncombined (UDUC) processing technique of the observations [18–20]. This can allow the detection and exclusion to be performed for individual faulty observations. This advantage is not available when, for example, the double differencing (DD) approach is used or when a grouping technique is applied where the whole satellite's observations (or a cluster of satellites) are removed once a suspected observation is detected [21,22]. Some IM schemes have been proposed when using PPP-RTK as a positioning technique [23–25]. However, these studies used least squares (LS) and EKF as processing techniques where neither adaptive nor robust functions are used which poses the limitations mentioned earlier. Therefore, CAKF has been suggested in this research as a processing filter in combination with PPP-RTK.

The main contribution of this research is proposing a combined positioning and IM approach feasible for AVs using PPP-RTK, owing to its advantages. The proposed approach includes utilizing CAKF, which can significantly reduce the IM computational load by merging the fault detection with the position estimation processes. This is achieved through performing a robustness test epoch-wise, as a part of CAKF, for the received observations. The robustness test substitutes the time-consuming traditional methods of fault detection such as solution separation (SS) and Chi-square tests that are performed during the IM process and require testing of numerous subsets to identify faulty observations. In addition, CAKF adaptively updates the stochastic model of the observations at each epoch. The variance of the observations of the current epoch will be checked and adjusted based on the quality of the measurements assessed by their standardized residuals. This could produce more realistic results for the IM protection level that are neither optimistic nor overly conservative. Another way to create a conservative observation covariance matrix is by performing overbounding to the observation residuals collected over a long time, as discussed in Elsayed et al. [26]. This remains restricted to the environment in which the measurements were observed and overbounded. Another contribution of this research is proposing a new criterion to improve the computation of the standardized residual by introducing the adaptive UWV, which is the main parameter used to perform the robustness test. This would assist in making the robustness test more representative, and correspondingly, the protection level (PL) estimation would be tighter, i.e., improve availability of IM.

In this study, the next two sections will explain more regarding the UDUC concept and how PPP-RTK is applied on both the network and the user sides. They also discuss the theory of the proposed method and estimation technique. The fourth section encompasses an illustration of the testing methodology and the experimental testing of the proposed method. The results are presented with a comprehensive discussion in the fifth section. Finally, the conclusion and the proposed future work are provided in the last section.

2. PPP-RTK Operation Concept and Observation Equations

PPP-RTK uses a network of reference stations that can estimate ionosphere and troposphere corrections (the wet part of the troposphere), satellite clocks and phase biases. In this research, the dry part of the troposphere has been modelled on both the network and user sides. The corrections are transmitted to users within the coverage area of the network. The users can, therefore, estimate their state vector and fix the ambiguities quickly. More details are provided in Khodabandeh et al. [27]. On the network side for each epoch (t), we have the following observation model:

$$y_{net_t} = A_{net_t} a_{net_t} + e_{net_t} \tag{1}$$

where y_{net_t} is the code and phase observations vector of the network stations; A_{net_t} is a full-rank Jacobian matrix which depends on geometry of the satellites relative to the users; a_{net_t} is the unknowns' vector that includes the observations corrections, which are estimated and transmitted to users including phase biases, ionospheric corrections, and clock offsets of the satellites; e_{net_t} is the measurement noise vector. The observation model for the user side then reads:

$$y_{U_t} - V_{U_t} a_{U_t} = B_{U_t} b_{U_t} + e_{U_t} \tag{2}$$

where y_{U_t} is the observation vector of the user; V_{U_t} is the full-rank design matrix of the corrections vector a_{U_t} that is interpolated from the corrections received from the network; B_{U_t} is the full-rank Jacobian matrix of the user's vector of unknowns b_{U_t}; and e_{U_t} is the user measurement noise vector. In this study, we considered the use of dual-frequency GNSS observations by both the network and the user. The form of multi-frequency scenarios can also be flexibly expanded as discussed in Odijk et al. [28].

The UDUC observation equations for PPP-RTK for the network side can be expressed as:

$$E(C_R^s) = c\left(\bar{t}_R - \bar{t}^s\right) + \overline{T}_{R_W} + \mu_i \overline{I}_{R_i}^s \tag{3}$$

$$E(\varphi_R^s) = c\left(\bar{t}_R - \bar{t}^s\right) + \overline{T}_{R_W} - \mu_i \overline{I}_{R_i}^s + \frac{c}{f_i}\overline{N}_{R_i}^s + \bar{\delta}_{R_i} - \bar{\delta}_i^s \tag{4}$$

where $E(.)$ is the expected value of the observed minus computed terms where the network position coordinates are fixed to their known values; C_R^s, φ_R^s are pseudorange code and phase observations (in m); s, R refer to the observed satellite and the receiver, respectively; c represents the speed of light; t_R, t^s are the receiver and satellite clock offsets, respectively; $(\bar{\cdot})$ denotes a certain representation of the parameters used to eliminate rank deficiencies by using the S-system theory [18], as shown in Table 1.

T_{R_W} is the wet part of the tropospheric delay in the line-of-sight direction; $I_{R_i}^s$ represents the ionosphere delay on the first frequency; f_i is the frequency of the observed signal i; $\mu_i = f_1^2 / f_i^2$ is the frequency-dependent ionosphere multiplier factor; $N_{R_i}^s$ is the phase ambiguity; δ_{R_i} *and* δ_i^s are the receiver and satellite phase biases, respectively; M is the master station among the reference stations; $d_{R_{IF}}$ and $d_{M_{IF}}$ represent the ionosphere-free (IF) linear combinations of the code biases for the reference station (R) or master station (M); $d_{R_{GF}}$ and $d_{M_{GF}}$ are the geometry-free (GF) linear combinations of the code biases for R or M [19]; d_{IF}^s and d_{GF}^s are the IF and GF linear combinations of the code biases for satellite s; $\lambda_i = c/f_i$; and s_P denotes the pivot satellite among the observed satellites.

Table 1. PPP-RTK parameterization of the network model.

Parameter	Definition
$\bar{t}_R$	$t_R - t_M + \left(d_{R_{IF}} - d_{M_{IF}}\right)/c$
$\bar{t}^s$	$t^s - t_M + \left[d^s_{IF} - d_{M_{IF}} - T_{M_w}\right]/c$
$\overline{T}_{R_W}$	$T_{R_W} - T_{M_W}$
$\overline{I}^s_{R_i}$	$I^s_{R_i} + d_{R_{GF}} - d^s_{GF}$
$\overline{N}^s_{R_i}$	$\left(N^s_{R_i} - N^s_{M_i}\right) - \left(N^{s_P}_{R_i} - N^{s_P}_{M_i}\right)$
$\bar{\delta}_{R_i}$	$\left(\delta_{R_i} - d_{R_{IF}} + \mu_i d_{R_{GF}} + \lambda_i N^{s_P}_{R_i}\right) - \left(\delta_{M_i} - d_{M_{IF}} + \mu_i d_{M_{GF}} + \lambda_i N^{s_P}_{M_i}\right)$
$\bar{\delta}^s_i$	$\delta^s_i - d^s_{IF} + \mu_i d^s_{GF} - \delta_{M_i} + d_{M_{IF}} - \mu_i d_{M_{GF}} - \lambda_i N^s_{M_i}$

The user can apply the PPP-RTK processing technique by exploiting the corrections provided by the network, where at the user end:

$$E\left(C^s_U + c\left(\bar{t}^s\right) - \mu_i I^s_{net\,i}\right) = r^s_U + c\left(\bar{\bar{t}}_U\right) + \overline{T}_{U_W} + \mu_i \bar{\bar{d}}_{U_{GF}} + e^s_{U_C} \tag{5}$$

$$E\left(\varphi^s_U + c\left(\bar{t}^s\right) + \bar{\delta}^s_i + \mu_i I^s_{net\,i}\right) = r^s_U + c\left(\bar{\bar{t}}_U\right) + \overline{T}_{U_W} + \lambda_i \overline{N}^s_{U_i} + \bar{\bar{\delta}}_{U_i} + \epsilon^s_{U_\varphi} \tag{6}$$

where U is the user receiver; $I^s_{net\,i}$ is the interpolated ionospheric correction provided by the network; r^s_U represents the range between satellite s and the user; $e^s_{U_C}$, $\epsilon^s_{U_\varphi}$ are the noises of code and phase observations, respectively, that may include location-dependent errors such as multipath; ($\bar{\bar{.}}$) denotes a representation applied by the user to eliminate the rank deficiency using the S-system theory, as shown in Table 2. The uncertainty of the network corrections has been neglected due to their insignificant effect except for the uncertainty of the interpolated ionospheric correction that has been considered in the observation stochastic model.

Table 2. PPP-RTK parameterization of the user model.

Parameter	Definition
$\bar{\bar{t}}_U$	$[t_U + (d_{U_{IF}}/c)] - [t_M + (d_{M_{IF}}/c)]$
$\bar{\bar{d}}_{U_{GF}}$	$d_{U_{GF}} - d_{M_{GF}}$
$\bar{\bar{\delta}}_{U_i}$	$\left(\delta_{U_i} - d_{U_{IF}} + \lambda_i N^{s_P}_{U_i}\right) - \left(\delta_{M_i} - d_{M_{IF}} + \lambda_i N^{s_P}_{M_i}\right)$

3. Estimation Method

In the case of using EKF as the estimating process, the equations of the prediction step are briefly listed and expressed as:

$$X_t = \Phi_{t|t-1}\hat{X}_{t-1} \tag{7}$$

$$P_{X_t} = \Phi_{t|t-1} P_{\hat{X}_{t-1}} \Phi^T_{t|t-1} + \mathcal{Q}_{t|t-1} \tag{8}$$

where X_t denotes the predicted state estimate, which is an incremental increase to initial values; $\phi_{t|t-1}$ is the linearized state transition matrix that connects the user parameters in two consecutive epochs; $\hat{X}_{t-1}$ is the estimated state vector of the previous epoch that contains position components, phase ambiguity, receiver clock error, and receiver code and phase biases; P_{X_t} is the covariance matrix of the predicted state vector; $P_{\hat{X}_{t-1}}$ is the covariance matrix of the estimated state vector of the previous epoch; and $\mathcal{Q}_{t|t-1}$ is the covariance

matrix of the process noise. The Kalman gain (K_t) is computed, and the measurement update is applied as follows:

$$K_t = P_{X_t} B_t^T \left[B_t P_{X_t} B_t^T + Q_{y_t} \right]^{-1} \tag{9}$$

$$P_{\hat{X}_t} = (\mathrm{I} - K_t B_t) P_{X_t} \tag{10}$$

$$\Delta \hat{X}_t = X_t + K_t [\Delta y_t - B_t X_t] \tag{11}$$

where B_t is the Jacobian matrix; Q_{y_t} is the measurement covariance matrix; I is the identity matrix; $\Delta \hat{X}_t$ is the difference in the estimates from the previous iteration; and Δy_t refers to the observed minus computed observation term. The process is repeated iteratively.

In the above equations, if the covariance matrix of process noise $\mathcal{Q}_{t|t-1}$ is considered constant, it may not well represent the actual maneuvers and acceleration variations during a kinematic scenario. This will degrade the estimate of the covariance matrix of the predicted state vector P_{X_t}, and accordingly, the final state vector estimates $\hat{X}_t$. Therefore, it is important to adjust the contribution of the predicted state vector in the estimation process of the updated state vector $\hat{X}_t$ at each epoch, as explained next. This can be achieved by using an adaptive factor θ integrated in the Kalman gain estimation. First, we compute the standardized differences between the predicted state vector X_t and least squares (LS) estimate of the state vector $\check{X}_t$ using only the measurements of the current epoch, computed as follows [15]:

$$\Delta X_t = \frac{\| \check{X}_t - X_t \|}{\sqrt{tr(P_{X_t})}} \tag{12}$$

$$\Delta \check{X}_t = \left(B_t^T Q_{y_t}^{-1} B_t \right)^{-1} B_t^T Q_{y_t}^{-1} \Delta y_t; \quad \check{X}_t = \check{X}_0 + \Delta \check{X}_t \tag{13}$$

$$\theta = \begin{cases} \simeq 0 & |\Delta X_t| > \mho_2 \\ \frac{\mho_1}{|\Delta X_t|} \left(\frac{\mho_2 - |\Delta X_t|}{\mho_2 - \mho_1} \right)^2 & \mho_1 < |\Delta X_t| \leq \mho_2 \\ 1 & |\Delta X_t| \leq \mho_1 \end{cases} \tag{14}$$

where $\check{X}_0$ is the initial value in the iteration process to estimate $\check{X}_t$; $tr(.)$ is the trace of the matrix; $\mho_1$ and $\mho_2$ are constants of empirical values that range between 1 and 1.5 and between 3 and 4.5, respectively, based on several studies including vehicular trips in urban areas [9,15,16]. Choosing lower values for $\mho_1$ and $\mho_2$ indicates reduced confidence in the dynamic model's ability to accurately represent the actual movements. On the other hand, selecting higher values is appropriate for static positioning or when the dynamic model is more advanced and better able to capture the true motion. The adaptive factor θ will be used to modify the Kalman gain (later in Equation (21)). In addition to the adaptation of Kalman Filter, a change to the observation covariance matrix will take place (as shown in Equation (19)). A more realistic observation covariance matrix for every epoch will be updated based on the actual quality of the observations. This is performed through a robustness test for data screening of outliers, i.e., a one-sample *t*-test carried out for each observation based on its standardized residual in comparison to the rest of the observations from the same observation type. The selection of the *t*-test is due to the small number of observations considered in each observation type that results in a degree of freedom of less than 30 [29]. In this test, any outlier observations shall be significantly de-weighted by extremely inflating their variance. The variance of other observations is either kept as is or adjusted using a factor. This would reduce the risk of the adverse effect of including faulty observations in the model. This process can act as an alternative for the traditional time-consuming fault detection tests commonly used in IM processes such as SS and Chi-square tests.

The residual of each observation is standardized using the unit weight variance (UWV) of the respective observation type, i.e., L1 GPS code, L1 GPS phase, L2 GPS code, L2 GPS phase, and similarly for other constellations. This is because similar observations in the zenith direction are most likely to share the same properties that may be different from other types of observations. Unlike previous research studies, in which UWV has been computed epoch-wise using the residuals of the predicted estimate, we propose using the residuals of the updated solution, i.e., after the measurement update, of the predecessor epoch since this is expected to provide more representative residuals compared to the predicted ones. We also suggest an accumulative computation of UWV, so that the UWV will be enhanced every epoch by including additional residuals from consecutive epochs. The accumulative method of calculating the UWV is expected to make it representative and shall lead to a more reliable robustness test. However, the longer the data accumulation is, the more time it takes to process the data and perform the robustness test. This does not satisfy the need for quick real-time positioning estimation and IM processes. Therefore, a sliding window approach including a certain number of epochs is used for accumulating the residuals for the UWV computation. This is applied such that once a certain number of epochs is reached, the data of the earliest epoch will be disregarded and replaced by the data of the latest epoch. This is also important since the change between positioning environments could impact the residual values and their correlation with older data, which affects the UWV representation. The UWV for each observation type (υ^J) is calculated as follows:

$$\hat{v}_{t-1} = y_{t-1} - B_{t-1}\hat{X}_{t-1} \tag{15}$$

$$Q_{\hat{v}_{t-1}} = Q_{y_{t-1}} - B_{t-1}P_{\hat{X}_{t-1}}B_{t-1}^T \tag{16}$$

where $\hat{v}_{t-1}$ and $Q_{\hat{v}_{t-1}}$ are the residuals and their covariance matrix of the updated estimate from the previous epoch. Therefore, the UWV for each observation type equals:

$$\upsilon^J = \frac{\sum_{H=t-h}^{t-1}\left(\hat{v}^T Q_{\hat{v}}^{-1}\hat{v}\right)^J}{\sum_{H=t-h}^{t-1} n^J}, \quad if\ t \le h, H = 1 \tag{17}$$

where h is the sliding window length (number) of epochs; n^J is the number of observations of a certain type at any epoch. The standardized residual $(\overline{v}_t)_i^J$ of the observation i collected at the current epoch of observation type J equals:

$$(\overline{v}_t)_i^J = \frac{(\check{v}_t)_i^J}{\sqrt{\upsilon^J (Q_{\check{v}_t})_i^J}} \tag{18}$$

where $\check{v}_t$ and $Q_{\check{v}_t}$ are the residuals and their covariance matrix based on the LS estimate of the measurements y_t as per Equation (13). To calculate the updated covariance matrix of the observations, the following test is carried out. The outcome of this test is one of three decisions for each observation. Either (1) keep the observation variance the same as the pre-assumed value if the test statistic is below a selected lower threshold; (2) adjust the variance of the observation by a factor in case the test statistic lies between the upper and lower thresholds; (3) extremely inflate the variance of the observation such that they are practically not included in the solution if the test statistic is larger than the upper threshold [15]:

$$\left(\overline{q}_{y_t}\right)_i^J = \begin{cases} \simeq 0 & \beta_i^J > \psi_{2_{(\alpha_2, df^J)}} \\ \left(q_{y_t}\right)_i^J \left(\frac{\psi_{1_{(\alpha_1, df^J)}}}{\beta_i^J}\left(\frac{\psi_{2_{(\alpha_2, df^J)}} - \beta_i^J}{\psi_{2_{(\alpha_2, df^J)}} - \psi_{1_{(\alpha_1, df^J)}}}\right)\right)^{-1} & \psi_{1_{(\alpha_1, df^J)}} < \beta_i^J \leq \psi_{2_{(\alpha_2, df^J)}} \\ \left(q_{y_t}\right)_i^J & \beta_i^J \leq \psi_{1_{(\alpha_1, df^J)}} \end{cases} \tag{19}$$

where $\left(\overline{q}_{y_t}\right)_i^J$ is the entry for observation i of type J in an improved covariance matrix $\overline{Q}_{y_t}$; $\left(q_{y_t}\right)_i^J$ is the entry for observation i in the classical covariance matrix Q_{y_t}; ψ_1 and ψ_2 are critical values of the t-test at selected significance levels α_1 and α_2 and the computed degrees of freedom df^J for the observation type J that the tested observation belongs to; β_i^J represents the test statistic for the observation i (see right-hand side of Equation (19)). β_i^J equals the signal over noise [30] expressed as:

$$\beta_i^J = \frac{\left(\overline{v}_t\right)_i^J - \sum_1^{n^J-1} \frac{\left(\overline{v}_t\right)_j^J}{n^J-1}}{\left|\sum_1^{n^J-1}\left(\sum_1^{n^J-1} \frac{\left(\overline{v}_t\right)_j^J}{n^J-1} - \left(\overline{v}_t\right)_j^J\right)\right| / \sqrt{n^J-2}}, \qquad j = 1 \ldots n^J, j \neq i \tag{20}$$

The balancing factor θ computed in Equation (14) and the improved observation covariance matrix $\overline{Q}_{y_t}$ are used in the computation of the Kalman gain as follows:

$$\widetilde{K}_t = \frac{1}{\theta} P_{X_t} B_t^T \left[\frac{1}{\theta} B_t P_{X_t} B_t^T + \overline{Q}_{y_t}\right]^{-1} \tag{21}$$

$$\widetilde{P}_{\hat{X}_t} = \left(\mathrm{I} - \widetilde{K}_t B_t\right) P_{X_t} \left(\mathrm{I} - \widetilde{K}_t B_t\right)^T + \widetilde{K}_t \overline{Q}_{y_t} \widetilde{K}_t^T \tag{22}$$

One of the important outcomes of applying the aforementioned procedure is the creation of an observation covariance matrix that is representative of the work environment instead of the traditional method of using a nominal covariance matrix. This would provide more realistic covariance with precise bounding which may lead to a more representative PL and improve the decisions regarding the availability of IM as well as positioning reliability. The robustness test is carried out iteratively until no further adjustment is required for the weight of any observation. Otherwise, the user can define a certain number of iterations after which the integrity would be declared unavailable if the weights of the observations keep needing adjustment, reflecting the existence of a fault.

4. Experimental Testing Description

To validate the proposed method, dual frequency observations from multiple GNSS constellations have been collected at the CUT0 continuously operating reference station (CORS) at Curtin University, Australia representing the user side of the test. Figure 1 shows the names and locations of the stations used to apply PPP-RTK positioning in this study. Table 3 gives information about the network stations, observed frequencies and constellations, etc.

Figure 2 describes the proposed approach by a flowchart illustrating the processing sequence. It shows how the presented robustness test replaces the traditional FDE process. It also shows how calculating the UWV using the final and accumulated residuals of the predecessor epochs $(\hat{v}_{t-1})$ affects the input every epoch.

Table 3. Data collection strategy for testing the proposed method in PPP-RTK processing.

Parameter	Value
# of network stn.	10 CORS
Distance between network and user stn.	3~32 km
User receiver/receiver model	CUT0 at Curtin University/Trimble NetR9
GNSS constellations/frequencies	GPS-L1/L2: C1C, L1C, C2W, L2W
	Galileo-E1/E5b: C1X, L1X, C7X, L7X
	BDS-B1/B2: C2I, L2I, C7I, L7I
User sampling interval	1 s

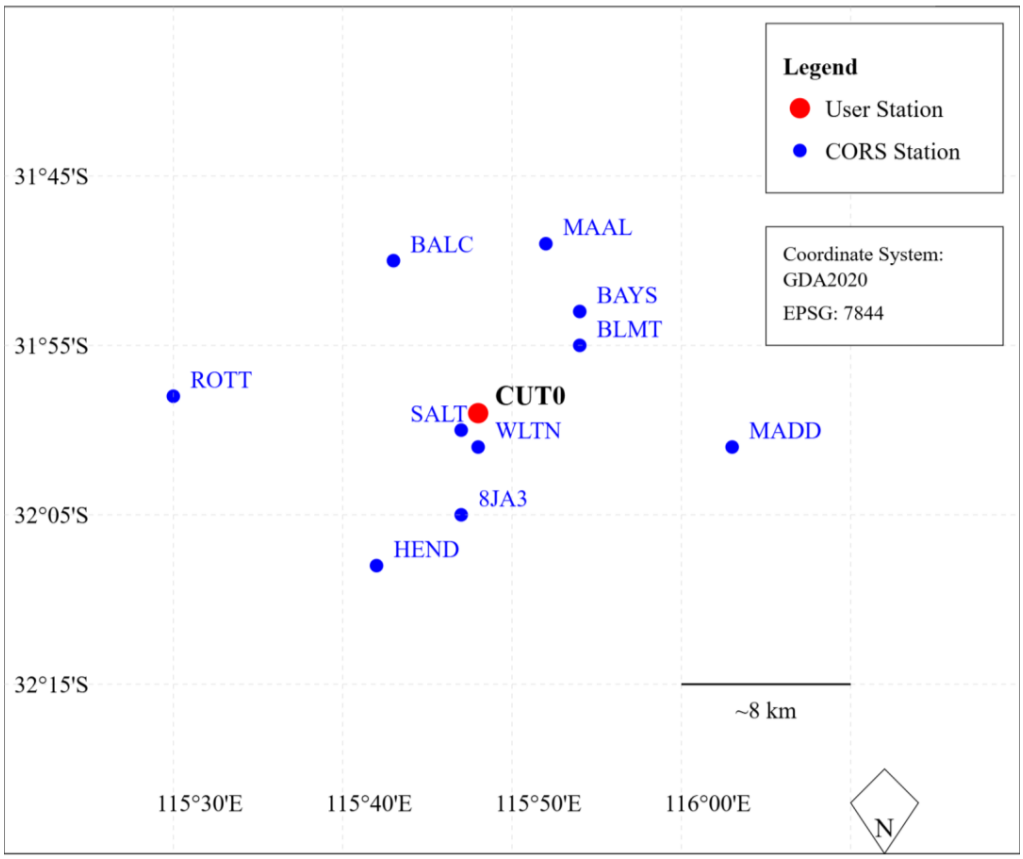

Figure 1. CORS stations used in applying PPP-RTK positioning.

In the test, the proposed adaptive UWV was computed using the sliding window approach that accumulates data up to a certain number of epochs $\sum_{t-h}^{t-1}(\hat{v}_{t-1})$ and compared to two previous methods to show the effect of using accumulated residuals. These two methods are (1) discrete UWV $(\hat{v}_{t-1})$, computed using the data from the current epoch only, which is the method used in most literature studies [15–17]; (2) accumulated UWV $\sum_{1}^{t-1}(\hat{v}_{t-1})$, computed using all data collected during the whole positioning period.

To determine the length of the suggested sliding window approach for the adaptive UWV, we studied the autocorrelation of the UWV over time for different observation types. The selected time delay is the one that corresponds to an autocorrelation factor (ACF) of 0.3, which is set as a threshold of low correlation. In real-time applications, accumulated UWV data can initially be used in the robustness testing with a fixed sliding window length (e.g., 100 epochs) while continuing to store additional data. After sufficient data are

collected, the ACF is analyzed to determine an optimal sliding window length, which is capped to ensure suitability for real-time use. The smaller of this cap (e.g., 5–10 min) or the ACF-based length is then applied, and this sliding window length is computed once for the duration of each positioning session.

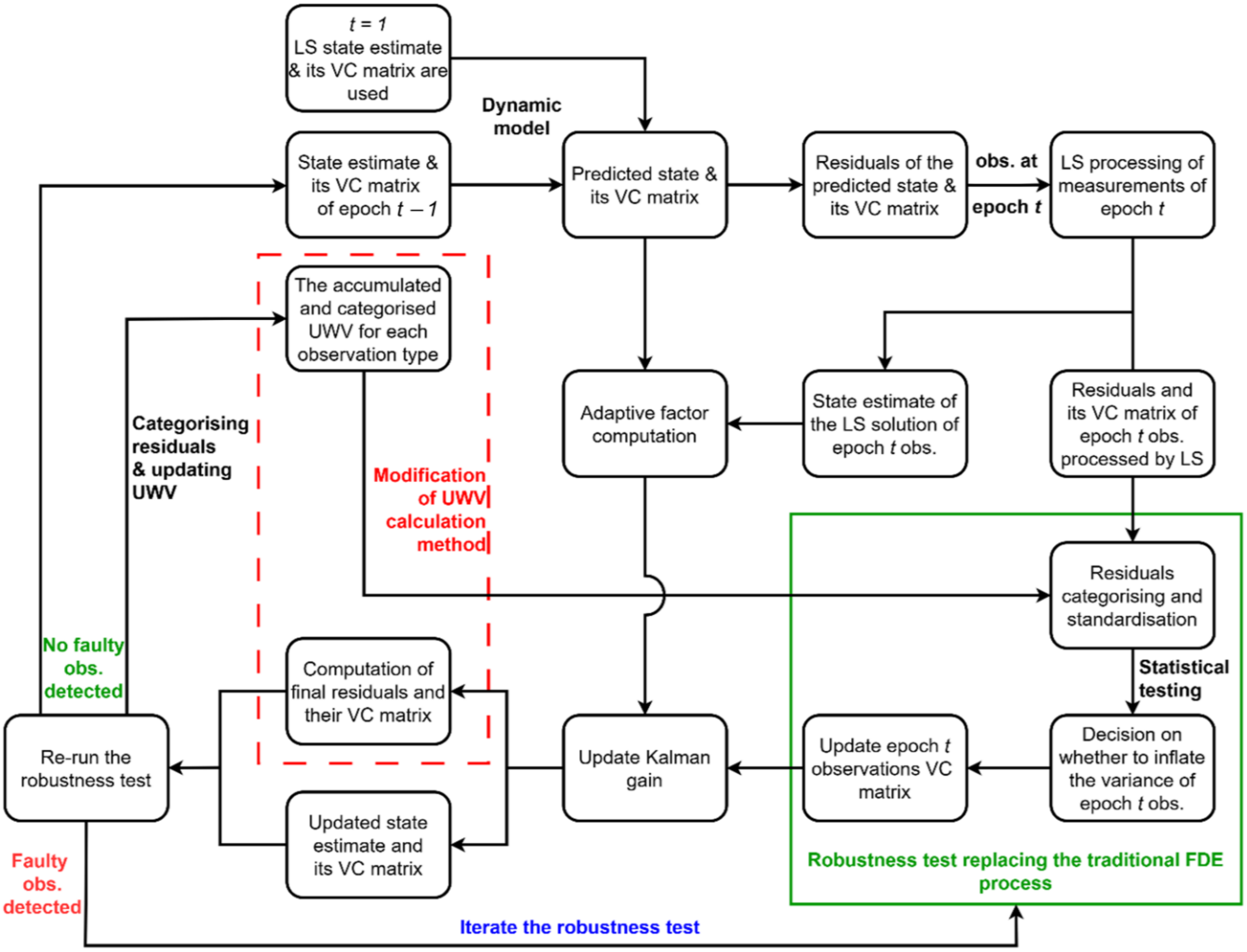

Figure 2. Flowchart of the processing sequence using CAKF in PPP-RTK concerning FDE and UWV computation.

To examine the CAKF in terms of its capacity to detect and identify faulty observations, three test cases are performed. For the first and second test cases, up to four simultaneous faults were injected at 30 s intervals throughout a one-hour positioning period. Significance levels of 0.1 and 0.001 were used in the *t*-test for the lower and the upper thresholds, respectively. We first performed the test with one injected fault in each of the tested epochs. Then, in separate tests, two, three, and four simultaneous faults were injected in each of the tested epochs. In the first test case, faults that range from 5 to 20 m were injected into code observations (representing code outliers), while faults ranging from 0.4 to 1 m were injected into phase observations (expressing undetected cycle slips ranging from two to five cycles). In the second test case, the range of the injected code outliers was from 120 to 200 m, and from 50 to 100 cycles for phase observations. Table 4 lists a sample of the observations into which the faults were injected during the first test case. The table includes the satellite PRN where faults were injected, the frequency and observation type, the fault value, and the epoch number in which each fault was injected.

To test the sensitivity of the CAKF in detecting smaller faults, the third test case was conducted in which two small code faults ranging from 1 to 5 m alongside two phase faults ranging from two to five cycles (making four faults in total) have been injected in their respective observation type every 30 s. Although small faults would have little impact on the position estimate, it is important to remove as many as possible of the small faults since applications such as AVs require in-lane accuracy. Furthermore, a longer observation period of about 10 h was processed twice where the upper significance level was changed (i.e., 0.001 and 0.0005). The purpose of testing different significance levels is to examine their effect on fault detection. Table 5 gives details of this test case.

Table 4. Details of a sample of the synthetically injected faults (in meters) into different observations and epochs in test case 1.

Epoch(s) #	One Fault			Two Faults			Three Faults			Four Faults		
	Satellite PRN/Observation type and frequency/Injected fault value (m)											
60	G12	C1C	6	E34	L7X	≈1	C02	C7I	12	C09	L2I	≈0.5
120	G30	L2W	≈1	C10	C7I	10	E27	L1X	≈1	G17	C1C	20
180	E02	C7X	15	G14	L1C	≈1	C03	C2I	7	G15	L2W	≈1
240	C01	C2I	20	E08	C7X	5	G19	L1C	≈0.5	C04	L7I	≈0.5
300	C11	L2I	≈1	G24	L2W	≈0.5	C12	C2I	5	E34	C7X	17
	← Two simultaneous faults →											
	← Three simultaneous faults →											
	← Four simultaneous faults →											

Table 5. Testing parameters for the third test case.

Parameters		Value	
Observation period (hr)		~10	
Frequency of fault injection (epoch)		30 s	
No. of injected faults/epoch	Code Obs.	2	
	Phase Obs.	2	
Size of injected faults	Code Obs. (m)	1–5	
	Phase Obs. (cycle)	2–5	
Total No. of injected faults		4520	
Upper significance level		0.001	0.0005
Lower significance level		0.1	

Finally, CAKF was compared to other commonly used methods, i.e., SS, Chi-square and Detection, Identification and Adaptation (DIA). The comparison includes the required time for the identification process, represented by the number of iterations required to identify the fault(s). Table 6 lists the probability assumptions of the statistical tests used in this research.

Table 6. Probability assumptions of DIA and the tested FDE methods in the first and second test cases.

	DIA/SS/Chi-Square	CAKF	
Significance level (s)	0.001	Upper threshold	0.001
		Lower threshold	0.1

5. Results and Discussion

To select the sliding window length, the ACF of the accumulated UWV was studied for a time delay of up to 1700 epochs for the considered observation types and GNSS constellations. From Figure 3, a low-med ACF of 0.3 was selected for which a maximum of 500 epochs is estimated as a conservative window length.

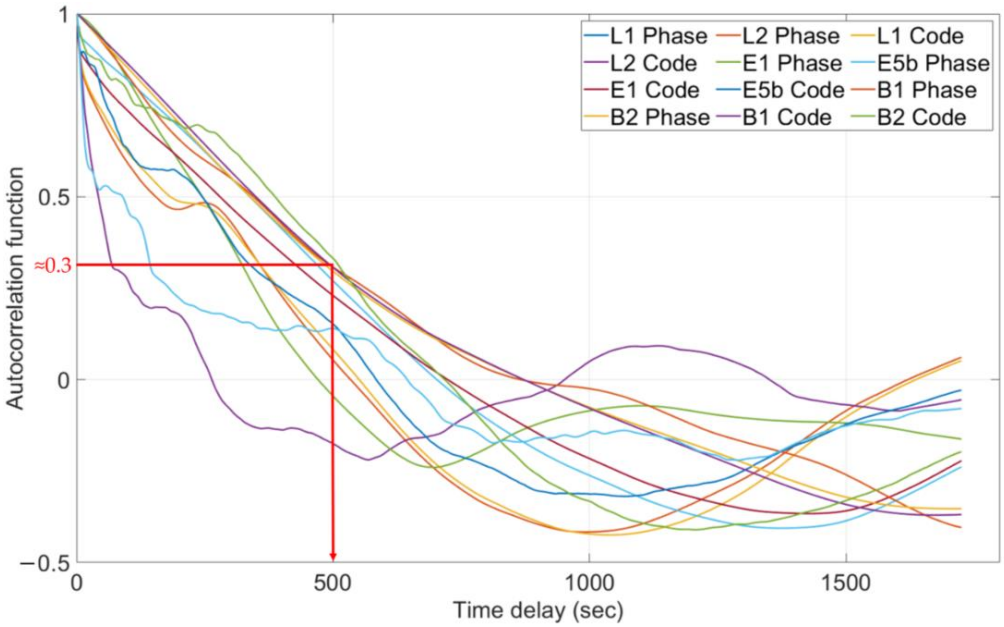

Figure 3. Autocorrelation function of the accumulated UWV over time for different observation types of different GNSS systems.

Figures 4 and 5 show the three different types of the computed UWV for code and phase observations, respectively. The three types are the discrete UWV computed using the data of the current epoch only, the accumulated UWV computed using data from the start of positioning up to the current epoch, and the adaptive UWV computed using data within the sliding window length. The UWV is computed for the utilized dual frequencies of each constellation.

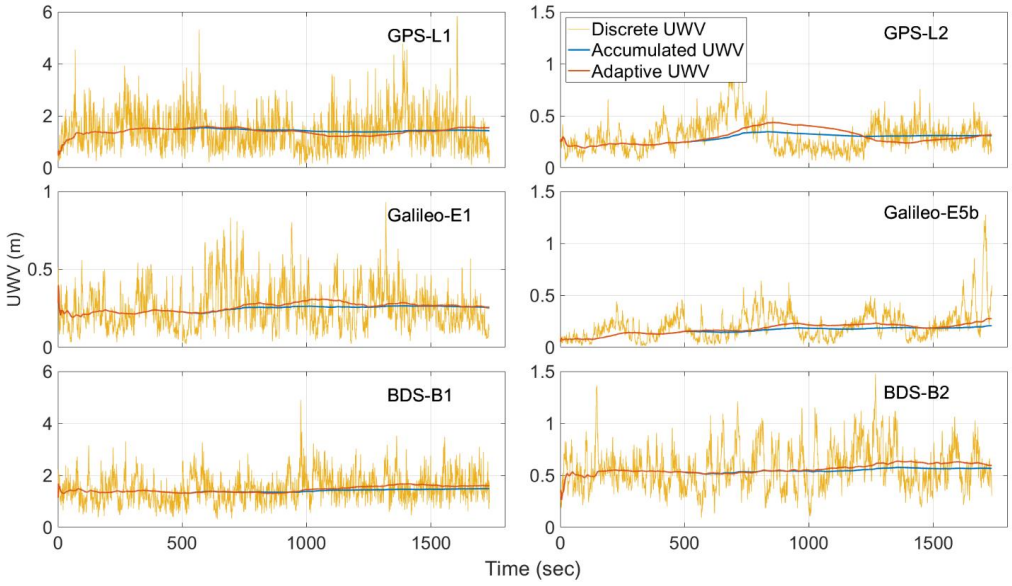

Figure 4. The three estimated types of UWV, i.e., discrete UWV, accumulated UWV, and adaptive UWV for code observations. Each row from top to bottom represents a constellation, i.e., GPS, Galileo, and BDS, respectively.

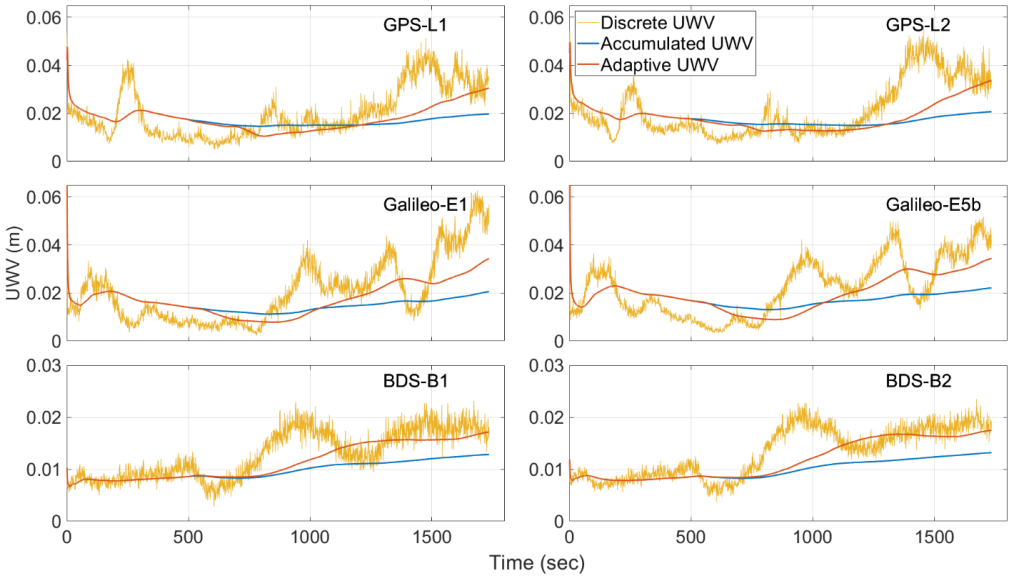

Figure 5. The three estimated types of UWV, i.e., discrete UWV, accumulated UWV, and adaptive UWV for phase observations. Each row from top to bottom represents a constellation, i.e., GPS, Galileo, and BDS, respectively.

As can be seen in the figures, the adaptive UWV computed using the sliding window is identical to the accumulated UWV until both methods reach 500 epochs, i.e., the selected limit for the sliding window technique before the old data starts to be overwritten by the recent one. Then, a small deviation takes place between the computed UWV by the two methods. The sliding window technique disregards the old residuals gradually that are less correlated with the current epoch in favor of fresh ones, which leads to an adaptive computation of the UWV. This would lead to a more representative UWV that considers the changes in the residuals due to changes in the operation environments or atmospheric conditions. On the other hand, the discrete UWV computed based on epoch-by-epoch residuals fluctuates. Such fluctuation can cause variations in the standardization process of the residuals as per Equation (18). Consequently, the outcome of the robustness test might be adversely affected. Table 7 summarizes the computed root mean square (RMS) of the UWV for each observation type of each constellation for an observing period of about 30 min. The table shows that the RMS of the discrete UWV is larger than the adaptive UWV by 7–28%, which would affect residual standardization when carried out.

Figures 6 and 7 show the variance adjusting factor assigned to each observation at three different sample epochs, i.e., epochs 60 s, 180 s, and 300 s when applying CAKF for FDE (Note that by applying UDUC, we have 4 observations per satellite and about 25 satellites per epoch, giving $\approx$ 100 observations per epoch). The two figures show the results of the first test case where the injected faults ranged from 0.4 to 20 m for phase and code observations, respectively. Figure 6 represents the scenario in which only one synthetic fault has been injected at each of the three presented epochs for the tested satellites listed in Table 4, while Figure 7 shows the scenario in which four simultaneous synthetic faults were injected in each of the three presented epochs. The details of the synthetically injected faults that are studied in Figures 6 and 7 are given in Table 4. A semi-log scale is used in the figures to accommodate the huge difference between the assigned adjusting factors between faulty and fault-free observations. The adjusting factor for the observations, whose test statistic exceeded the upper critical value of the robust test, has a value of 10^7 and is represented by the asterisk in the figures. The adjusting factor in this case is applied to the variance of all extremely de-weighted observations, so that they are practically not considered in the model, as explained in Equation (19). On the other hand, the observations

whose test statistics were between the upper and lower critical values during the robust test are represented in the figures by the triangle. The variance adjusting factor of these observations has a variable value that is more than one and up to different values that are computed as per Equation (19). The rest of the observations whose test statistic was below the lower critical value during the robust test, represented as dots in the figures, have their variance adjusting factor equal to one. Therefore, no change to the allocated elevation angle-dependent variance of these observations is applied. Figure 8 shows the variance adjusting factors of all observations at all epochs during one hour of positioning where four simultaneous synthetic faults were injected, as per the second test case procedure regarding the fault value and injection frequency.

Table 7. RMS of UWV of each observation type from different constellations.

GNSS System/ Frequency	Obs. Type	Obs. Frequency	RMS (m)		
			Discrete UWV	Adaptive UWV	Accumulated UWV
GPS L1/L2	Code	C1C	1.6065	1.4037	1.4226
		C2W	0.3461	0.3033	0.2885
	Phase	L1C	0.0227	0.0186	0.0175
		L2W	0.0240	0.0193	0.0179
Galileo E1/E5b	Code	C1X	0.2900	0.2576	0.2463
		C7X	0.2533	0.1826	0.1611
	Phase	L1X	0.0246	0.0188	0.0158
		L7X	0.0252	0.0211	0.0180
BDS B1/B2	Code	C2I	1.5834	1.4575	1.4028
		C7I	0.6023	0.5608	0.5413
	Phase	L2I	0.0136	0.0119	0.0099
		L7I	0.0140	0.0123	0.0101

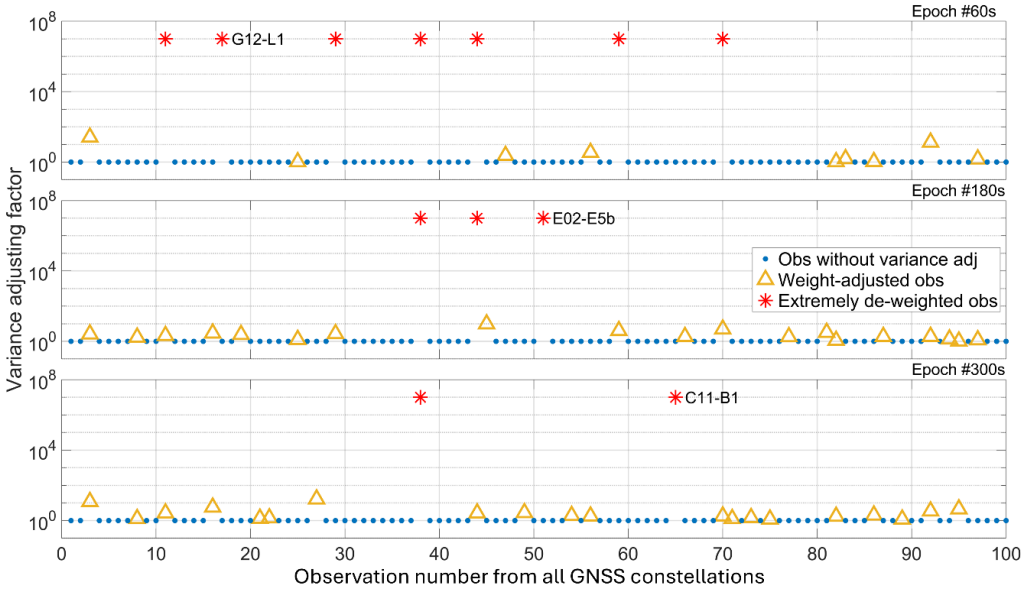

Figure 6. The variance adjusting factor of the observations at three different epochs, where one synthetic fault ranging from 0.4 to 20 m has been injected at each of the three epochs for the satellites listed in Table 4. The variance of the observations is either extremely inflated (asterisk), adjusted (triangle), or remained as the pre-assumed value (dot).

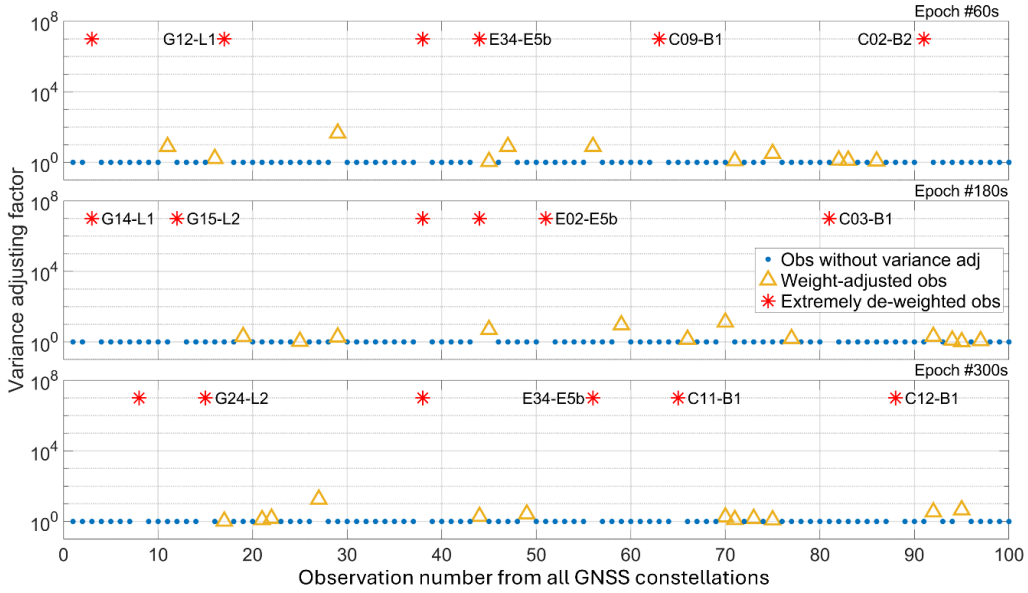

Figure 7. The variance adjusting factor of the observations at three different epochs, where four synthetic faults ranging from 0.4 to 20 m have been injected at each of the three epochs for the satellites listed in Table 4. The variance of the observations is either extremely inflated (asterisk), adjusted (triangle), or remained as the pre-assumed value (dot).

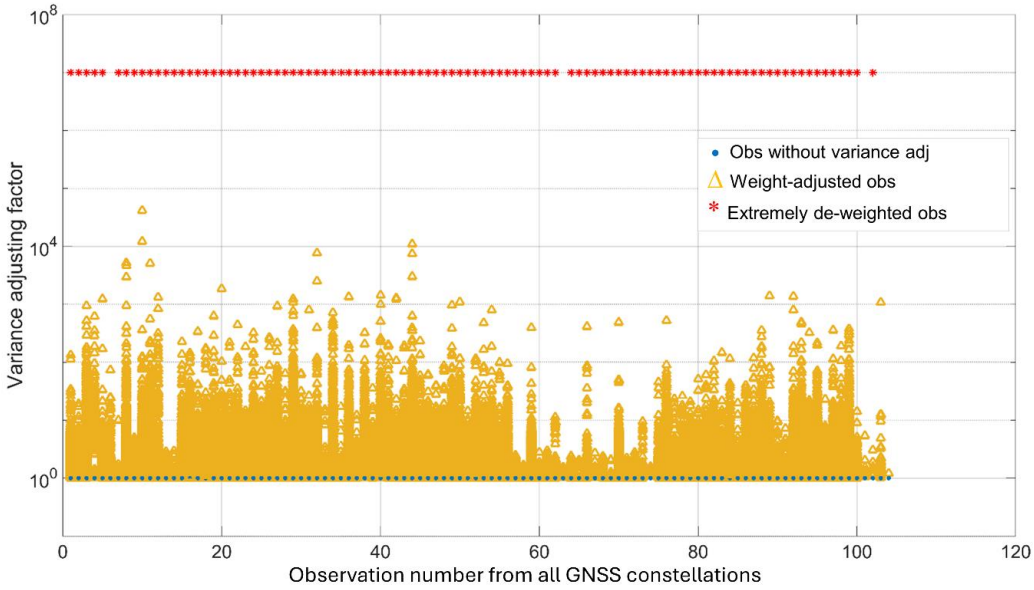

Figure 8. The variance adjusting factor of the observations for a positioning period of 1 h, where four synthetic faults ranging from 10 to 200 m have been injected every 30 s. The variance of the observations is either extremely inflated (asterisk), adjusted (triangle), or remained as the pre-assumed value (dot).

In the first and second test cases, CAKF successfully detected and identified all the observations with synthetic faults during different scenarios of injecting up to four simultaneous faults without additional iterations. The labelled observations in Figures 6 and 7 are those with injected faults as per Table 4. The variance of all identified observations has been inflated by a factor and hence has no or insignificant impact on the solution. Table 8 shows the advantage of the CAKF method in saving the computational load compared to other methods, such as iterative DIA, Chi-square, and SS. It lists the number of iterations and subsets that need to be processed in each method to identify the faulty observations, which is the same for the two test cases. This number changes in relation to the considered

number of simultaneous faults and the number of observations per epoch, which is around 100 observations in the test. The traditional Chi-square and SS methods were tested to detect and identify the case of one fault per epoch, and they successfully identified the faulty observation. Testing cases with two, three, and four simultaneous faults using SS and Chi-square methods was not performed, as processing the thousands of required subsets, as indicated in Table 8, is impractical for real-time positioning applications. While iterative DIA was able to detect and identify all faults up to four simultaneous ones, the number of iterations increased with the number of simultaneous faults.

Table 8. Number of additional processed subsets for fault identification using different FDE methods.

Method		One Fault	Two Faults	Three Faults	Four Faults
CAKF		1	1	1	1
Iterative DIA		1	2	3	4
Traditional Chi-2		100	5050	161,800	3,921,325
Solution Separation (SS)		100	5050	161,800	3,921,325
Computation saving when using CAKF (%)	DIA	0	50	67	75
	SS/Chi-2	99	99.999	99.999	99.999

As listed in Table 8, the computational load saving when applying CAKF is massive compared to other methods. It decreases the number of iterations, or the subsets required for processing from 50% to 99.999% based on the comparison method and the considered number of simultaneous faults. The number of additional subsets requiring processing in Table 8 for iterative DIA or Chi-square methods is only required when a detection test indicates a potential fault. In contrast, SS and CAKF methods conduct detection and identification tests simultaneously, necessitating the processing of the additional subsets in Table 8 at every epoch for these two methods. Note that all methods require additional computations to perform the detection test before or after (to confirm full exclusion of faulty observations) the identification process.

In the third test case, we examined CAKF's ability to detect and identify smaller faults as per Table 6. During an observation period of more than 10 h and almost 5000 injected faults, the proposed method detected and identified up to 85% of the injected faults when the upper significance level in Equation (19) was set to 0.001, while about 87% of the injected faults were detected and identified with an upper significance level of 0.0005. These detection and identification results are after the first iteration, as explained in Figure 2. Due to the large number of observations and the small size of the injected faults, the impact of the undetected faults is minor on the position estimate; hence, no more CAKF iterations were performed.

Looking at the current methods, when SS is used for aviation, for example, multipath is rarely anticipated. In addition, only epoch-wise smoothed code GPS observations are processed since the required alert limit is set to tens of meters [31,32]. Furthermore, the exclusion is performed per satellite. All of these conditions have resulted in limiting the number of subsets that need to be processed for fault identification, in case one or more simultaneous faults are suspected. On the other hand, ground applications such as AVs need many more observations in real time to preserve availability. Fault exclusion is best performed per observation, not per satellite, preserving the information of most observations in particular where the UDUC method is adopted. AVs require at least lane precision (< 1 m) for the estimated position, which necessitates the inclusion of phase observations. In addition, a large multipath is highly possible when navigating in urban areas. Therefore, it is very likely to have many simultaneous faults at any single epoch

due to cycle slips, no line of sight, or large multipath. Hence, methods such as SS and Chi-square will require the processing of a huge number of subsets, as shown in Table 8, unlike the proposed method.

Results show that the CAKF is efficient in detecting and identifying faulty observations. In addition, it reduced the computational load required for FDE compared to the other tested methods. The quality of the estimated position is also maintained. Figure 9 illustrates the position error in the three directions, i.e., east, north, and up, when one hour of data was processed after fault injection, as per the first test case where four simultaneous faults that range from 0.4 to 20 m were injected into code and phase observations every 30 s. The data were processed in three different modes where (1) no FDE method was used, (2) iterative DIA was implemented, and (3) CAKF was applied. The test was repeated and is presented in Figure 10, but in this case, the fault values increased to range from 10 to 200 m, as per the second test case criteria. Figures 11 and 12 present the position error in the three directions of the third test case, where four faults that range from 0.4 to 5 m were injected into phase and code observations every 30 s. The figures show the position error of both CAKF and iterative DIA for more than 10 h of observation. A significance level of 0.001 was used in the detection test of both methods in Figure 11, while the significance level was 0.0005 in Figure 12.

The results of Figure 9 show that the position error was at the decimeter level for both horizontal directions, and up to a meter in the vertical direction when no FDE method was used. The position error dropped to the centimeter level in the horizontal and vertical directions when iterative DIA was used. CAKF provided better results where the maximum position error was 3 and 10 mm for the horizontal and vertical directions, respectively. Figure 10 presents the increase in the position error up to a few meters when no FDE method was in use. With the implementation of iterative DIA, centimeter accuracy was maintained in both horizontal and vertical directions. The maximum position error was 6 and 11 mm in the horizontal and vertical directions when CAKF was applied.

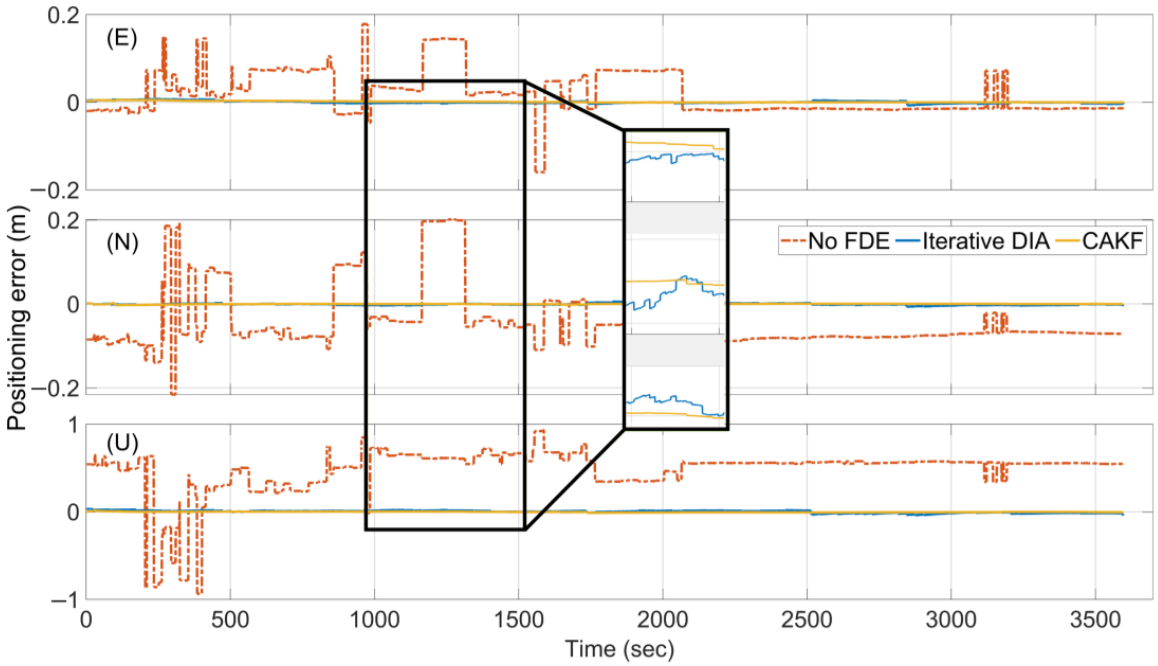

Figure 9. Position error in east, north, and up (different vertical axis scale) directions of CUT0, from top to bottom, respectively. Processing of the first test case was conducted using (1) no FDE, (2) iterative DIA, and (3) CAKF. The inset shows the results of methods (2) and (3).

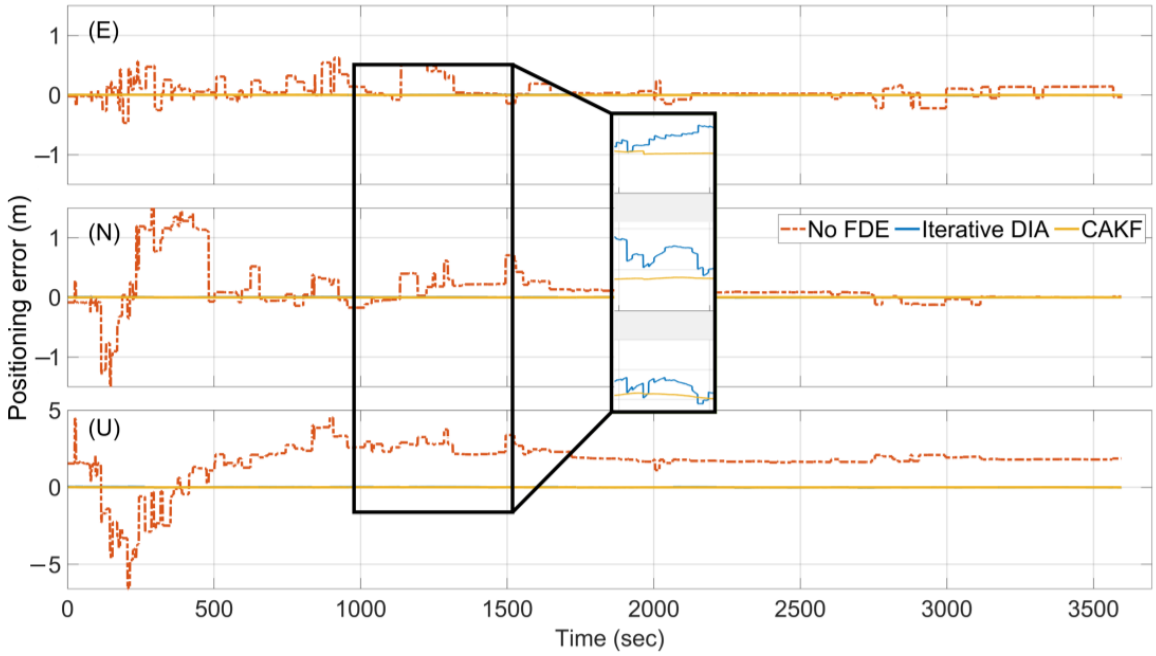

Figure 10. Position error in east, north, and up (different vertical axis scale) directions of CUT0, from top to bottom, respectively. Processing of the second test case was conducted using (1) no FDE, (2) iterative DIA, and (3) CAKF. The inset shows the results of methods (2) and (3).

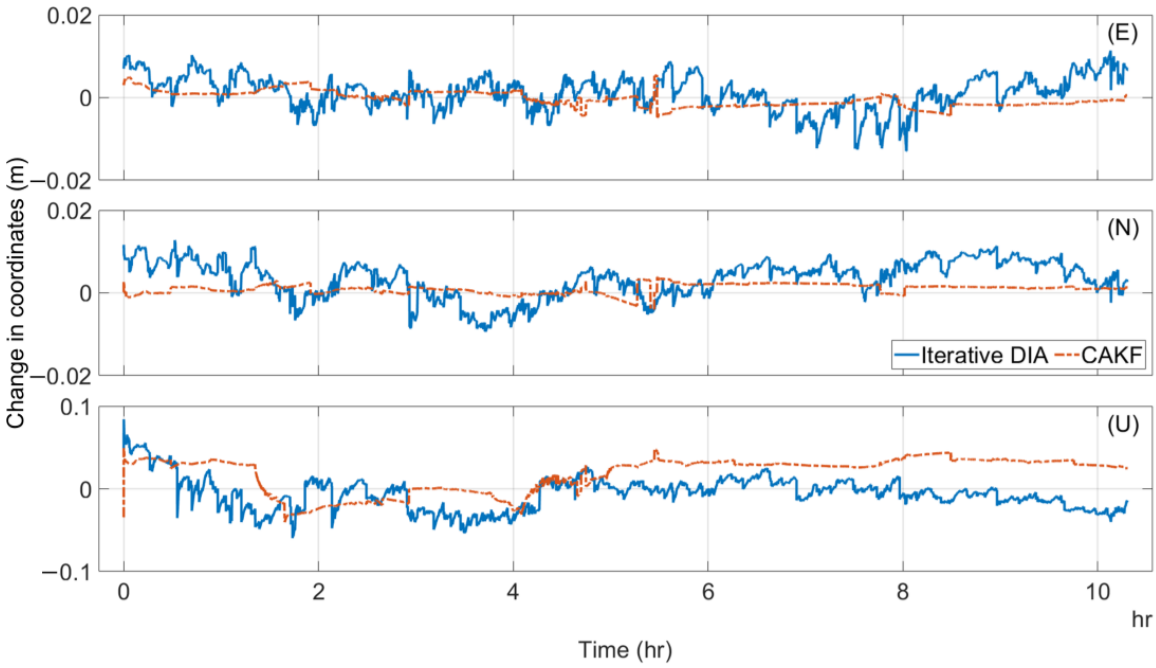

Figure 11. Position error in east, north, and up (different vertical axis scale) directions of CUT0, from top to bottom, respectively. Processing of the third test case was conducted with a significance level of 0.001 using (1) iterative DIA and (2) CAKF.

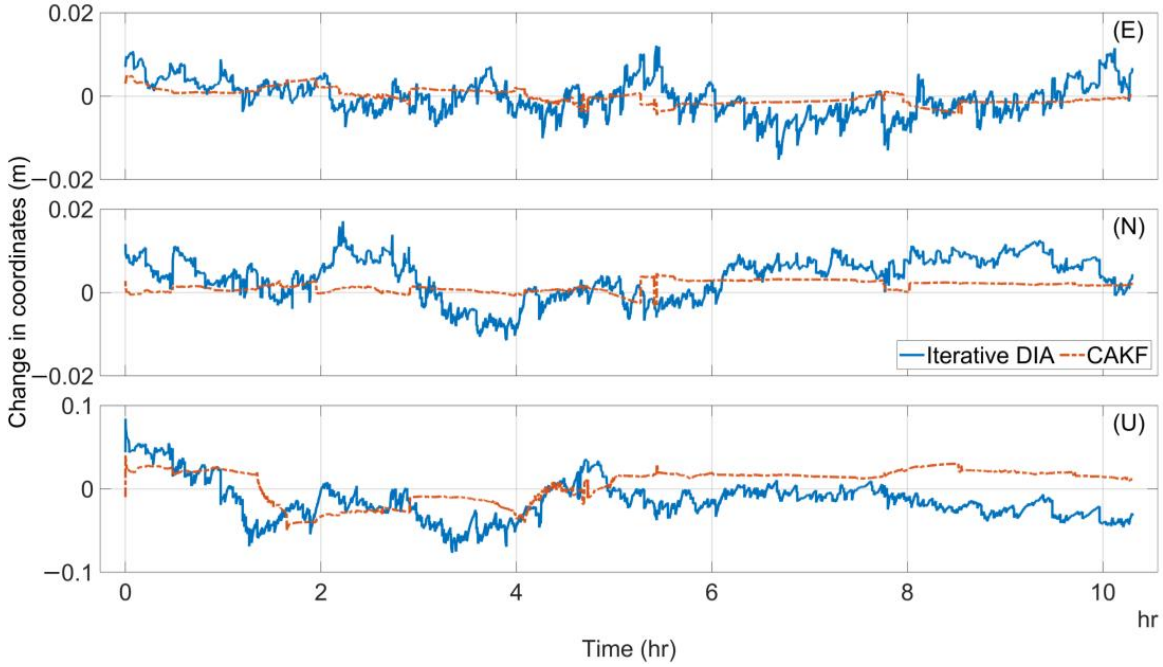

Figure 12. Position error in east, north, and up (different vertical axis scale) directions of CUT0, from top to bottom, respectively. Processing of the third test case was conducted with a significance level of 0.0005 using (1) iterative DIA and (2) CAKF.

In the first test, where the significance level was set to 0.001, Figure 11 shows a position error of about 5 mm in both horizontal directions and 5 cm in the vertical direction when CAKF was applied, while these values almost doubled when DIA was used. Similar position errors were obtained from both methods when the significance level was set to 0.0005, as shown in Figure 12. This demonstrates that a significance level of 0.001 was stringent enough to detect and identify all significant faulty observations. Although further tightening the level to 0.0005 led to more suspected faulty observations being excluded, as mentioned earlier, it did not improve the positioning estimate, indicating that these additional exclusions did not significantly impact position quality. The case of No FDE was excluded from the third test case, as its effect was already represented in the first and second test cases. This allowed better representation of the comparison between the proposed CAKF and iterative DIA over a longer testing period. The three test cases show the ability of the proposed method in efficiently detecting, identifying and handling a wide range of simultaneous code and phase faults.

6. Conclusions and Future Work

Positioning with FDE of ground applications such as AVs is proposed using PPP-RTK processed with an improved CAKF. PPP-RTK provides reliable and real-time positioning using UDUC observations without the need for the traditional RTK setup or performing double differencing. CAKF alleviates adverse effects of the fixed covariance matrix of the dynamic model, when EKF is used, by balancing the contribution of both prediction and estimation steps. The CAKF approach includes the implementation of a robustness test for outlier detection and de-weighting of suspected observations. This test can function as an alternative to the commonly used FDE methods, which are computationally expensive and may not be suitable for real-time positioning. CAKF also encompasses an updating process for the observation stochastic model every epoch. This enhances the production of a realistic observation covariance matrix, and consequently, more representative IM parameters such as PL. We also suggested a salient modification to the method of computing the UWV, which

represents a major parameter of the robustness test. Whilst UWV was computed using single epoch predicted residuals and re-computed every epoch, a sliding time window was proposed where the estimated residuals of the most recent consecutive epochs for a certain period are used. The length of the sliding window was pre-set based on an autocorrelation study of the UWV over time. This modification provided more representative UWV that improved the subsequent computations of the robustness test.

The suggested modification to the computation of UWV was examined for different observation types of different constellations. Three types of UWV were computed: (1) discrete UWV, (2) accumulated UWV, and (3) adaptive UWV. Results showed a considerable fluctuation in the discrete UWV values, whereas the adaptive UWV residuals were steady, with a reduction of 7–28% in the RMS compared to the discrete UWV. The CAKF robustness test was examined in terms of its capacity to detect and identify various simultaneous faults. In the first test case, synthetic faults in code and phase, ranging from 5 to 20 m and from two to five cycles respectively, were injected into the observations every 30 s. The second test case involved larger fault injections, with code faults between 120 and 200 m and phase faults between 50 and 100 cycles. To investigate the performance of the method for FDE of small faults, a third test case spanned over 10 h, with smaller code faults (1 to 5 m) and phase faults (two to five cycles) injected every 30 s throughout the testing period. CAKF successfully identified and de-weighted all observations with injected faults in the first and second test cases. Up to 87% of faulty observations were detected in the latter test case with a minor impact on the position solution. The quality of the estimated position was maintained when CAKF was used for FDE. The largest position error was about 6 and 11 mm in the horizontal and vertical directions, during the three test cases. In terms of computational load saving, CAKF reduced the number of iterations and subsets that are required for fault identification by 50% to 99.999% compared to the classical SS, Chi-square, and iterative DIA. This reduction percentage varies based on the comparison method and the considered number of simultaneous faults.

Future research will focus on enhancing the applicability of the proposed method in real-world scenarios. A key aspect of this effort is improving the PPP-RTK infrastructure, which could involve network densification through an increased number of reference stations and enhancing the quality of corrections provided to users. This approach has the potential to improve FD capabilities and minimize the number of simultaneously faulty satellites that users need to consider for exclusion, thus reducing computational demands and increasing the practicality of the method.

Additionally, future investigations will include testing the method using kinematic positioning data in challenging environments where many faults due to cycle slips and loss of lock may take place. Future work also incorporates the computation of the PL to check the effect of the proposed technique on IM availability, and the possibility of improving the performance.

Author Contributions: H.E.: Conceptualization, Methodology, Software, Validation, Formal analysis, Investigation, Resources, Data Curation, Writing—Original Draft; A.E.-M.: Conceptualization, Methodology, Resources, Writing—Review and Editing, Supervision; A.A.-Z.: Software, Writing—Review and Editing; K.W.: Writing—Review and Editing, Supervision; X.M.: Software, Writing—Review. All authors have read and agreed to the published version of the manuscript.

Funding: This research is supported by the Australian Research Council, grant number (DP240101710) to the second co-author, the International Partnership Program of the Chinese Academy of Sciences (CAS), grant number (021GJHZ2023010FN) and National Natural Science Foundation of China, grant number (12473078) to the fourth co-author.

Data Availability Statement: The datasets generated during and/or analyzed during the current study are available from the corresponding author upon reasonable request.

Acknowledgments: The first author acknowledges the Egyptian Ministry of Higher Education and Scientific Research for providing him with a scholarship to complete his PhD studies at Curtin University, Australia, and the School of Earth and Planetary Sciences, Curtin, University for partial support of this study. The authors acknowledge HxGN SmartNet for providing access to Australian GNSS network data used in this study. The support of the Australian Research Council is acknowledged by the second co-author. The fourth co-author acknowledges the International Partnership Program, CAS and National Natural Science Foundation of China, for their support.

Conflicts of Interest: The authors declare no conflicts of interest. The funders had no role in the design of the study; in the collection, analyses, or interpretation of data; in the writing of the manuscript; or in the decision to publish the results.

References

1. Joubert, N.; Reid, T.G.; Noble, F. Developments in modern GNSS and its impact on autonomous vehicle architectures. In Proceedings of the 2020 IEEE Intelligent Vehicles Symposium (IV), Las Vegas, NV, USA, 19 October–13 November 2020; pp. 2029–2036. [CrossRef]
2. Jing, H.; Gao, Y.; Shahbeigi, S.; Dianati, M. Integrity Monitoring of GNSS/INS Based Positioning Systems for Autonomous Vehicles: State-of-the-Art and Open Challenges. *IEEE Trans. Intell. Transp. Syst.* **2022**, *23*, 14166–14187. [CrossRef]
3. Hassan, T.; El-Mowafy, A.; Wang, K. A review of system integration and current integrity monitoring methods for positioning in intelligent transport systems. *IET Intell. Transp. Syst.* **2021**, *15*, 43–60. [CrossRef]
4. El-Mowafy, A.; Wang, K. Integrity monitoring for kinematic precise point positioning in open-sky environments with improved computational performance. *Meas. Sci. Technol.* **2022**, *33*, 085004. [CrossRef]
5. El-Mowafy, A.; Wang, K.; El-Sayed, H. Integrity Monitoring for Network RTK Users with Enhanced Computational Performance. In Proceedings of the 35th International Technical Meeting of The Satellite Division of the Institute of Navigation (ION GNSS+ 2022), Denver, CO, USA, 19–23 September 2022; pp. 1–10.
6. Elsayed, H.; El-Mowafy, A.; Wang, K. A new method for fault identification in real-time integrity monitoring of autonomous vehicles positioning using PPP-RTK. *GPS Solut.* **2024**, *28*, 32. [CrossRef]
7. Hao, Y.; Xu, A.; Sui, X.; Wang, Y. A Modified Extended Kalman Filter for a Two-Antenna GPS/INS Vehicular Navigation System. *Sensors* **2018**, *18*, 3809. [CrossRef]
8. Mohamed, A.H.; Schwarz, K.P. Adaptive Kalman filtering for INS GPS. *J. Geod.* **1999**, *73*, 193–203. [CrossRef]
9. Yang, Y.; He, H.; Xu, G. Adaptively robust filtering for kinematic geodetic positioning. *J. Geod.* **2001**, *75*, 109–116. [CrossRef]
10. Hu, C.; Chen, W.; Chen, Y.; Liu, D. Adaptive Kalman filtering for vehicle navigation. *J. Glob. Position. Syst.* **2003**, *2*, 42–47. [CrossRef]
11. Ding, W.D.; Wang, J.L.; Rizos, C.; Kinlyside, D. Improving adaptive Kalman estimation in GPS/INS integration. *J. Navig.* **2007**, *60*, 517–529. [CrossRef]
12. Yang, Y.X.; Gao, W.G. An optimal adaptive Kalman filter. *J. Geod.* **2006**, *80*, 177–183. [CrossRef]
13. Li, M.; Nie, W.; Xu, T.; Rovira-Garcia, A.; Fang, Z.; Xu, G. Helmert Variance Component Estimation for Multi-GNSS Relative Positioning. *Sensors* **2020**, *20*, 669. [CrossRef] [PubMed]
14. Yang, Y.; Song, L.; Xu, T. Robust estimator for correlated observations based on bifactor equivalent weights. *J. Geod.* **2002**, *76*, 353–358. [CrossRef]
15. Zhang, Q.Q.; Zhao, L.D.; Zhao, L.; Zhou, J.H. An Improved Robust Adaptive Kalman Filter for GNSS Precise Point Positioning. *IEEE Sens. J.* **2018**, *18*, 4176–4186. [CrossRef]
16. Elmezayen, A.; El-Rabbany, A. Real-time GNSS precise point positioning using improved robust adaptive Kalman filter. *Surv. Rev.* **2021**, *53*, 528–542. [CrossRef]
17. Lotfy, A.; Abdelfatah, M.; El-Fiky, G. Improving the performance of GNSS precise point positioning by developed robust adaptive Kalman filter. *Egypt. J. Remote Sens. Space Sci.* **2022**, *25*, 919–928. [CrossRef]
18. Odijk, D.; Khodabandeh, A.; Nadarajah, N.; Choudhury, M.; Zhang, B.C.; Li, W.; Teunissen, P.J.G. PPP-RTK by means of S-system theory: Australian network and user demonstration. *J. Spat. Sci.* **2017**, *62*, 3–27. [CrossRef]
19. Zha, J.P.; Zhang, B.C.; Liu, T.; Hou, P.Y. Ionosphere-weighted undifferenced and uncombined PPP-RTK: Theoretical models and experimental results. *GPS Solut.* **2021**, *25*, 135. [CrossRef]
20. Zhang, B.C.; Chen, Y.C.; Yuan, Y.B. PPP-RTK based on undifferenced and uncombined observations: Theoretical and practical aspects. *J. Geod.* **2019**, *93*, 1011–1024. [CrossRef]

21. Orejas, M.; Skalicky, J.; Ziegler, U. Implementation and testing of clustered ARAIM in a GPS/Galileo receiver. In Proceedings of the 29th International Technical Meeting of the Satellite Division of the Institute of Navigation (ION GNSS+ 2016), Portland, OR, USA, 12–16 September 2016; pp. 1360–1367. [CrossRef]
22. Walter, T.; Blanch, J.; Enge, P. Reduced subset analysis for multi-constellation ARAIM. In Proceedings of the 2014 International Technical Meeting of the Institute of Navigation, San Diego, CA, USA, 27–29 January 2014; pp. 89–98.
23. Wang, K.; El-Mowafy, A.; Qin, W.; Yang, X. Integrity monitoring of PPP-RTK positioning; Part I: GNSS-based IM procedure. *Remote Sens.* **2021**, *14*, 44. [CrossRef]
24. Zhang, W.H.; Wang, J.L.; El-Mowafy, A.; Rizos, C. Integrity monitoring scheme for undifferenced and uncombined multi-frequency multi-constellation PPP-RTK. *GPS Solut.* **2023**, *27*, 68. [CrossRef]
25. Zhang, W.H.; Wang, J.L. Integrity monitoring scheme for single-epoch GNSS PPP-RTK positioning. *Satell. Navig.* **2023**, *4*, 10. [CrossRef]
26. Elsayed, H.; El-Mowafy, A.; Wang, K. Bounding of correlated double-differenced GNSS observation errors using NRTK for precise positioning of autonomous vehicles. *Measurement* **2023**, *206*, 112303. [CrossRef]
27. Khodabandeh, A.; Teunissen, P.J.G.; Psychas, D. On the Problem of Double-Filtering in PPP-RTK. *Sensors* **2022**, *23*, 229. [CrossRef]
28. Odijk, D.; Zhang, B.; Khodabandeh, A.; Odolinski, R.; Teunissen, P.J. On the estimability of parameters in undifferenced, uncombined GNSS network and PPP-RTK user models by means of S-system theory. *J. Geod.* **2016**, *90*, 15–44. [CrossRef]
29. Mishra, P.; Singh, U.; Pandey, C.M.; Mishra, P.; Pandey, G. Application of student's *t*-test, analysis of variance, and covariance. *Ann. Card. Anaesth.* **2019**, *22*, 407–411. [CrossRef]
30. Francis, G.; Jakicic, V. Equivalent statistics for a one-sample *t*-test. *Behav. Res. Methods* **2023**, *55*, 77–84. [CrossRef]
31. Blanch, J.; Walter, T.; Enge, P. RAIM with Optimal Integrity and Continuity Allocations Under Multiple Failures. *IEEE Trans. Aerosp. Electron. Syst.* **2010**, *46*, 1235–1247. [CrossRef]
32. El-Mowafy, A.; Yang, C. Limited sensitivity analysis of ARAIM availability for LPV-200 over Australia using real data. *Adv. Space Res.* **2016**, *57*, 659–670. [CrossRef]